

## *HST* astrometry in the 30 Doradus region: II. Runaway stars from new proper motions in the Large Magellanic Cloud

Imants Platais<sup>1</sup>, Daniel J. Lennon<sup>2</sup>, Roeland P. van der Marel<sup>3,1</sup>, Andrea Bellini<sup>3</sup>, Elena Sabbi<sup>3</sup>, Laura L. Watkins<sup>3</sup>, Sangmo T. Sohn<sup>3</sup>, Nolan R. Walborn<sup>3</sup>, Luigi R. Bedin<sup>4</sup>, Christopher J. Evans<sup>5</sup>, Selma E. de Mink<sup>6</sup>, Hugues Sana<sup>7</sup>, Artemio Herrero<sup>8</sup>, Norbert Langer<sup>9</sup>, Paul Crowther<sup>10</sup>

imants@jhu.edu

Received \_\_\_\_\_; accepted \_\_\_\_\_

---

<sup>1</sup>Department of Physics and Astronomy, Johns Hopkins University, 3400 North Charles Street, Baltimore, MD 21218, USA

<sup>2</sup>European Space Astronomy Centre, Camino bajo del Castillo, Urbanizacion Villafranca del Castillo, Villanueva de la Cañada, 28692, Madrid, Spain

<sup>3</sup>Space Telescope Science Institute, 3700 San Martin Drive, Baltimore, MD 21218, USA

<sup>4</sup>INAF-Osservatorio Astronomico di Padova, Vicolo dell'Osservatorio 5, I-35122 Padova, Italy

<sup>5</sup>UK Astronomy Technology Centre, Royal Observatory Edinburgh, Blackford Hill, Edinburgh, EH9 3HJ, UK

<sup>6</sup>Anton Pannekoek Institute for Astronomy, University of Amsterdam, Science Park 904, 1098 XH, Amsterdam, The Netherlands

<sup>7</sup>Institute of astrophysics, KU Leuven, Celestijnlaan 200D, 3001, Leuven, Belgium

<sup>8</sup>Instituto de Astrofísica de Canarias, 38200 La Laguna, Tenerife, Spain

<sup>9</sup>Argelander-Institut für Astronomie, Universität Bonn, Auf dem Hügel 71, 53121, Bonn, Germany

<sup>10</sup>Department of Physics and Astronomy, Hicks Building, Hounsfield Road, University of Sheffield, Sheffield S3 7RH, United Kingdom

## ABSTRACT

We present a catalog of relative proper motions for 368,787 stars in the 30 Doradus region of the Large Magellanic Cloud (LMC), based on a dedicated two-epoch survey with the Hubble Space Telescope (*HST*) and supplemented with proper motions from our pilot archival study. We demonstrate that a relatively short epoch difference of 3 years is sufficient to reach a  $\sim 0.1$  mas yr<sup>-1</sup> level of precision or better. A number of stars have relative proper motions exceeding a 3-sigma error threshold, representing a mixture of Milky Way denizens and 17 potential LMC runaway stars. Based upon 183 VFTS OB-stars with the best proper motions, we conclude that none of them move faster than  $\sim 0.3$  mas yr<sup>-1</sup> in each coordinate – equivalent to  $\sim 70$  km s<sup>-1</sup>. Among the remaining 351 VFTS stars with less accurate proper motions, only one candidate OB runaway can be identified. We rule out any OB star in our sample moving at a tangential velocity exceeding  $\sim 120$  km s<sup>-1</sup>. The most significant result of this study is finding 10 stars over wide range of masses, which appear to be ejected from the massive star cluster R136 in the tangential plane to angular distances from 35'' out to 407'', equivalent to 8-98 pc. The tangential velocities of these runaways appear to be correlated with apparent magnitude, indicating a possible dependence on the stellar mass.

*Subject headings:* astrometry – galaxies: Magellanic Clouds: individual (30 Dor)

## 1. INTRODUCTION

This study addresses new measurements of proper motions with *HST* for individual stars in the 30 Doradus (hereafter 30 Dor) area of the LMC in the context of a search for runaway OB stars and potential scenarios of how the massive OB stars formed. In our first paper by Platais et al. (2015), hereafter Paper I, we give the motivation to study this area and provide a detailed account how to obtain high-accuracy positions and relative proper motions with various *HST* imaging instruments. We demonstrate that it is possible to measure reliably an individual relative proper motion down to  $\sim 0.1 \text{ mas yr}^{-1}$ , which corresponds to  $\sim 25 \text{ km s}^{-1}$  at the distance of the LMC. As a result, we presented a pilot catalog of positions and relative proper motions, derived from a targeted single-epoch survey combined with numerous archival *HST* observations spanning up to 17 years. Although the precision of proper motions can be as good as  $\sim 20 \mu\text{as yr}^{-1}$ , the accuracy of proper motions appears to be significantly lower due to residual systematic errors. In addition, as indicated by Fig. 13 of Paper I, our pilot catalog has spatial discontinuities and covers only  $\sim 30\%$  of the available contiguous area.

In Paper I, we also attempted to identify possible runaway OB stars using the calculated proper motions for 86,590 stars. That resulted in six candidate OB proper-motion runaway stars. Interestingly, three of them are part of the VLT-FLAMES Tarantula Survey (VFTS; Evans et al. 2011), whereas, another three are additional photometric OB stars. We noted that star VFTS 285 appears to have its proper motion and position consistent with the ejection scenario from the massive star cluster R 136. Still, none of the astrometric candidate OB runaway stars could be considered as a conclusive case.

There are two studies of line-of-sight (LOS) velocities that also address potential OB runaway stars in the 30 Dor area and slightly eastward of it (Evans et al. 2015a,b). These authors identify a total of 18 candidate runaway stars. Assuming that none of them is a

large-amplitude binary, only five of them have an excess LOS velocity in the range  $75 < v_{\text{LOS}} < 108 \text{ km s}^{-1}$ , while the rest have lower velocities with the lowest one at  $40 \text{ km s}^{-1}$ . This range of excess LOS velocities implies that the expected total proper motion of true OB runaway stars may not exceed  $\sim 0.4 \text{ mas yr}^{-1}$ . The anticipated upper limit is still non-trivial to measure with *HST* over a time span of a few years. The concept of effective Point-Spread-Function (ePSF), accurate accounting for geometric distortions, and empirical correction for the effect of Charge Transfer Efficiency (CTE) losses are the three crucial developments that now allow us to measure relative positions of stars to the level of  $\sim 0.5 \text{ mas}$  (Anderson & King 2000, 2003; Anderson & Bedin 2010).

In addition, we designed the second epoch observations such that they matched the first-epoch observations as closely as possible, thus minimizing the contribution by the main source of systematic errors related to a star’s location on the detector and possible changes in signal-to-noise ratio between the epochs. The combined set of first- and second-epoch observations is analyzed here. There is an overlap in terms of the applied techniques and methods of analysis with Paper I and the reader is frequently directed to this paper. This is also true for the Introduction – a more detailed scientific motivation is provided in Paper I.

## 2. *HST* SURVEY OF 30 DOR AND DATA REDUCTIONS

One of the main goals in our astrometric survey was to use the Wide Field Camera 3 (WFC3/UVIS) and the Advanced Camera for Surveys (ACS/WFC) in parallel in order to cover as much of 30 Dor as possible, focusing in particular on the VFTS stars (Evans et al. 2011). The first epoch observations (GO-12499; PI: D. Lennon) were mainly obtained in 2011 October 3-8, while nearly identical second epoch observations (GO-13359) were repeated three years later in 2014, October 6-11. Details of the first epoch observations are given in Paper I. For the second-epoch observations, the last sub-pointing  $D$  in each

observational set (see Fig. 3, Paper I) has a small  $\sim 3\%$  adjustment to its exposure time and some pointings have different guide stars. As opposed to the first-epoch observations, in 2014 we did not apply preflash to ACS short exposures. For all practical reasons, both first and second epoch observations are nearly identical. Altogether, there is a total of 149 ACS/WFC and the same number of WFC3/UVIS frames, both sets obtained through filter F775W. Similar to Paper I, we used `_flc.fits` files. The latter are corrected for the effect of charge-transfer efficiency (CTE) losses in images (Anderson & Bedin 2010). We note that these corrections reflect the status of adopted pipeline procedures in the year 2015. At the time of this writing, some of them have been updated, thus now resulting in slightly different output of `_flc.fits` files.

It should be mentioned that the Hubble Tarantula Treasury Project (HTTP, Sabbi et al. 2016) is a rich source of additional observations in the 30 Dor area. Although the instrumental setup is identical to our program and include other filters such as F555W and F658N, there are differences in the visit pointings and orientation angles. This may introduce unwanted systematics if compared to our observations, which are *optimized* to exclude systematics in proper motions. Since these HTTP observations do not extend the available span of time coverage, we decided not to use them in our analysis.

The object detection, the calculation of their centroid, flux, quality parameter `qfit`, and correction for geometric distortion – all followed the guidelines provided in Paper I, Sect. 3.1.

### **2.1. Differential charge-transfer inefficiency**

Complementary to the CTE losses is the charge-transfer inefficiency (CTI) effect which is just another way of interpreting small offsets in the positions introduced during the CCD

readout process. Since all frames have been already corrected for the effect of CTE losses, we would expect that the residuals from a transformation of the second-epoch positions into the first-epoch positions do not contain any dependence on the magnitude of stars in the direction of CCD readout. If this is not true, then we name such a dependence to be a differential CTI, which in essence reflects the degree of CTE-correction efficiency.

First, we examined pairs of identical WFC3/UVIS first-to-second epoch pointings taken with the same exposure time. It is expected that a linear transformation (offset, rotation, and scale) of distortion-uncorrected centroids from one epoch to another would enable us to characterize the stability of star pixel coordinates over time. Due to the large distance of the LMC, the expected proper motions over three years have a very limited contribution to the total budget of positional errors. This exercise brought to light two issues: a small offset (a few hundredths of a pixel) between the two CCD chips and a slope in proper motions as a function of magnitude and the  $Y$  pixel location. The same pattern was discovered in the similar pairs of ACS/WFC frames. Small variations in the gap size between the chips are expected but they have no impact on proper motions because, in our final adjustment, each chip is transformed into the astrometric reference frame separately (Paper I, Sect. 3.2). The second issue is more serious. A slope in the  $Y$  pixel location as a function of magnitude appears to be a hallmark of some residual (differential) unaccounted-for CTE losses. It may appear odd to have this effect after the pipeline corrections for the CTE losses. However, Anderson & Bedin (2010) caution that the adopted empirical model for corrections may not be perfect. By comparing positions at, e.g., two epochs, we can actually test whether the adopted model might need a time-dependent component.

In order to build a statistically significant sample, we selected three sets of frames – 15 pairs taken with short exposure (35 s for WFC3/UVIS) of sub-pointing A (see Paper I, Fig. 3), 15 pairs with long exposures (699 s for WFC3/UVIS) of the same sub-pointing,

and 14 pairs of sub-pointing D with somewhat shorter exposure times (490-507 s for WF3/UVIS). Similarly, we selected the corresponding ACS/WFC pointings and exposures (see Paper I, Sect. 2). Then, for each pair we used least-squares minimization and a linear three-term polynomial to transform first-epoch positions into the system of second-epoch positions. In this transformation only positions of optimally-exposed stars were used (instrumental magnitudes in the range  $-14 < m_{F775W} < -8$ ) and obvious outliers ignored. In the next step, residuals of all matching stars were collected and assigned to the applicable CCD chip, which include precise pixel-location on that chip and measured instrumental magnitude.

To characterize differential CTI between the two epochs, the collection of individual residuals for each chip was re-distributed into successive bins of instrumental magnitude. The total number of available residuals per chip varies between  $\sim 15,000$  and  $\sim 150,000$  depending on the imager (WFC3 or ACS) and the length of exposure time. Each bin is at least 0.333 mag wide and is shifted by 0.2 mag with respect to the adjoining bin. The minimum number of residuals per bin is adopted to be 105. If a bin contains fewer residuals, it is enlarged until the required number is reached. This procedure is essential for the bright end of magnitude bins, where the number of stars is always low. Then, in each bin a least-squares fit is applied to the residuals in  $Y$ -coordinate as a function of  $Y$ . We used a linear 3-term polynomial which provides a potential slope in these residuals characterizing differential CT. We could not find statistically significant non-linearity in the actual fits. An example provided in Fig. 1 shows the general pattern of slopes as a function of magnitude, which reflects the presence of differential CTI. If this is ignored, then it will introduce a bias in the calculated proper motions.

In Figures 2,3 we show the maximum effect (at the far edge of a CCD chip) of differential CTI for both imaging instruments for short and long exposures. Formally,

the effect is dependent on the exposure time and is more pronounced on short exposures. The turnover at instrumental magnitude  $m_{F775W} \sim -8$  appears to be an artifact of the pixel-based pipeline correction applied to our images. We hope that these findings will provide stimulus to the further improvements in minimization of CTI effects on fluxes and positions. For this project, we applied differential CTI corrections to all second epoch frames.

In order to apply these corrections to distortion-uncorrected coordinates, we generated a total of 12 empirical CTI curves. That is, each one for a short, long, and an intermediate length (364-507 s) exposure; for each imaging instrument (ACS/WCS and WFC3/UVIS); and for each chip. We note that the shape and amplitude of the corresponding curves for long and intermediate exposures are quite similar, indicating that the differential CTI effect may not be linearly-correlated with the length of exposure. The raw distribution of slopes as a function of magnitude (Fig. 1) is too noisy and coarse to work with. Therefore, we iteratively smoothed these distributions and then applied cubic splines to parameterize the resulting curves (see Figs. 2, 3). For instrumental magnitudes of  $-15$  and brighter a zero correction was adopted. Also, differential CTI correction of any magnitude is adopted to be zero at the near-edge of a CCD readout direction. Once positions of the second-epoch frames were corrected for differential CTI, the resulting coordinates were then corrected for geometric distortion using the same routines and parameters as in Paper I.

We also explored the possibility of some differential CTI effect in the serial direction because Anderson & Bedin (2010) reported the presence of the so-called  $x$ -hook in the direction away from the readout amplifier. None was detected, although we did not attempt to explore that for each separate CCD amplifier.

## 2.2. New Proper Motions

In Paper I we described all basic steps on how to calculate proper motions using mosaic-like observations with three different *HST* imaging instruments. A central role in these calculations served the astrometric reference catalog, which covers the entire field-of-view (FOV). At the time of constructing this reference frame, we noticed a need for nonlinear terms in the transformation of the ACS/WFC positional catalog into the WFC3/UVIS-based positions and some semi-periodic systematics after this transformation. Therefore, with the arrival of second-epoch *HST* observations in 2014, we decided to use the WFC3/UVIS positional catalog as is, not including positions from the slightly overlapping parts of the ACS/WFC reference catalog. As a result, all WFC3/UVIS frame-solutions into its own reference catalog have significantly better rms for overlapping visits (pointings) 01-07 (see Fig. 2, Paper I). This is confirmed by the distribution of corresponding rms in both axes (Fig. 4). All WFC3/UVIS solutions yield small rms estimates and never exceed 0.025 pixel. We note that the second-epoch observations also include the contribution of proper motions over 3 years. Therefore, the second epochs clump near the rms of  $\sim 0.02$  pixel.

Similar solutions for the set of ACS/WFC frames show a noticeably different pattern. The rms of the first-epoch solutions, as expected, clump near 0.015 pixel but the second-epoch ACS/WFC frames obtained with 32 s exposure cluster around the considerably higher  $\sim 0.04$  UVIS pixel. Clearly, this is not due to the proper motions. First, we noticed that the image quality parameter `qfit` for nearly all ACS second-epoch frames is significantly elevated – up to twice that of the first-epoch relatively bright images. Despite using the same fiducial ePSFs as in Paper I, somehow the actual second-epoch stellar images may have slightly changed their shape, especially on frames with exposure time of 32 s, which are least appropriate to construct a new set of ePSFs. Second, the available

correction for geometric distortion of ACS/WFC frames may not be optimal as indicated by a necessity to apply a quadratic term in order to align with the WFC3/UVIS positions in constructing the astrometric reference catalog (Paper I). As a result, proper motions from ACS/WFC observations have somewhat lower precision and accuracy than those derived from the WFC3/UVIS observations. To alleviate the impact of potential residual geometric distortion, pixel positions on each chip for both, WFC3/UVIS and ACS/WFC, were separately translated into the astrometric reference frame.

New proper motions were calculated following the instructions given in Paper I, Sect. 3.3.2. As in Paper I, we used the same, effectively, a four-pixel box to find all common positions for a star on the system of the astrometric reference catalog. Since the epoch difference is three years, the chosen box size misses fast moving stars exceeding  $\sim 25$  mas yr<sup>-1</sup> in one coordinate. Likewise, we have proper motions from linear least-squares fits to the unweighted and weighted  $XY$  positions. In the final catalogs of proper motions only the "weighted" version of the proper motions is provided. The principal improvement in our current version of the proper motions is a complete coverage of the entire available FOV, while the spatial coverage in Paper I is patchy and represents only  $\sim 30\%$  of the total FOV.

The mean error of proper motions from WFC3/UVIS observations and for magnitude range  $14 < m_{F775W} < 20$  is 0.088 mas yr<sup>-1</sup> in either coordinate. This magnitude range contains all optimally-exposed OB stars. Similarly, for ACS/WFC observations in the same magnitude range, the mean error is 0.12 and 0.10 mas yr<sup>-1</sup> along RA and Dec, respectively. These larger errors as well as possible systematics in our astrometry lower the chances to detect OB runaways using the ACS/WFC data.

### 2.3. Catalogs of proper motions

Measuring *individual* proper motions in the LMC is close to the limits of any ground- or space-based facility’s state-of-the-art status, including the *Gaia* mission. Therefore, here we provide four catalogs of proper motions that give an opportunity to examine their internal consistency and other properties (Proper Motion Catalog, electronic Table). All our proper motion measurements are relative and effectively local. The mean motion of stars from the astrometric reference catalog should be zero. These proper motions might be used to establish upper limits on the internal velocity dispersion for selected stellar populations. However, their main advantage is the ability to identify faster moving stars.

In Paper I and here we have used four *HST* imagers: WFPC2 Planetary Camera (PC1), WFPC2 Wide Field, ACS/WFC, and WFC3/UVIS. In practice, it would be difficult to tease apart WFPC2’s PC1 data from its Wide Field contribution. Hence, the proper-motion catalog from Paper 1 represents mixed contribution by these WFPC2 cameras but it is possible to separate contribution by ACS/WFC from that from WFC3/UVIS, owing to their minimal spatial overlap. Proper motions and associated parameters from Paper I are marked by the suffix “c”. There are 86,606 such entries. The new proper motions and their parameters from ACS/WFC observations are marked by the suffix “a” (210,745 entries), and those from WFC3/UVIS observations – with “u” (165,737 entries). Finally, a catalog of combined proper motions (suffix “m”) represents an attempt to calculate weighted mean proper motions and their errors using available combinations of individual proper motions. We did not address the cases showing clear discrepancy in proper motion between two separate measurements, unless it is a potential runaway. The rule of thumb in such cases is that a smaller total proper motion is more likely to be true and the new proper motions from WFC3/UVIS measurements are the most reliable. We note that a number of brighter stars with the proper-motion measurement in Paper I are missing in the

new catalogs. This is because in Paper I we applied a universal image-cutoff threshold at the instrumental magnitude of  $m_{F775W} = -14.33$ , while in the study it was  $-14.0$  for long exposures by ACS/WFC and, similarly,  $-14.25$  for WFC3/UVIS frames. These changes helped to eliminate poor measurements of proper motion.

Each proper motion measurement comes with its standard error estimate, the number of datapoints, the calculated  $\chi^2$ , and the goodness-of-fit probability  $Q$ . Ancillary data include  $VI$  photometric data from Sabbi et al. (2016), rectangular  $XY$  coordinates aligned along the RA and Dec directions, Right Ascension and Declination (J2000). The total number of entries in the combined and collated proper-motion catalog is 368,787.

#### 2.4. Potential impact of *Gaia* DR 1

The all-sky *Gaia* Data Release 1 (DR 1; Gaia Collaboration et al. 2016) is an obvious dataset to compare with *HST* measurements. We retrieved a few thousand DR 1 sources near the cluster R136. There are issues with completeness of stars in the 30 Dor area and an apparent imbalance of positional errors. On average, the mean positional error in Right Ascension is  $\sim 4$  times smaller than that in Declination. It was decided to use only those stars with positional errors less than 2 mas in either coordinate, which limits the sample to  $\sim 2,000$  stars all brighter than  $G=19$ . First, we calculated J2000 equatorial coordinates for our astrometric reference catalog using the DR 1 stars as a reliable representation of the International Celestial Reference System (ICRS). We adopted a linear 6-parameter polynomial model to transform the pixel coordinates into the tangential coordinates of DR 1 stars. As demonstrated by Fig. 5, the calculated residuals contain significant systematics reaching up to  $\sim 50$  mas. If we consider only the WFC3/UVIS positions, then the corresponding residuals reach only  $\sim 7$  mas. This is a direct evidence that the positions from observations with ACS/WFC are not free from residual geometric

distortions. A similar conclusion has been reached from independent studies of an *HST* astrometric reference catalog based on ACS/WFC observations of the globular cluster 47 Tuc (Kozhurina-Platais et al. 2015). For the sake of proper motions in the 30 Dor area, the less than optimal accuracy of our ACS/WFC reference catalog is not as detrimental as it may look. The ACS/WFC CCD chip covers an area of  $3\frac{1}{4} \times 1\frac{1}{7}$  on the sky. Even the long side of a chip may be shorter than the characteristic length of correlated residuals, which is corroborated by the sub-mas standard errors in local solutions (Table 2, Paper I). Since the placing of second-epoch frames relative to first epochs normally is within a 1-2 ACS/WFC pixels, we used essentially the same reference stars for both epochs. These mitigating factors significantly lower the impact of an imperfect reference catalog.

We also explored whether the DR1 can be used as an additional epoch to improve the precision of proper motions. Note that the timing of our second epoch is  $\sim 2014.8$ , while for DR1 it is exactly 2015.0. That near simultaneousness ensures easy comparison between two sets of positions. Only the WFC3/UVIS frames and the corresponding WFC3/UVIS astrometric reference catalog were used. It is convenient to work in the system of our astrometric reference catalog. Therefore, we calculated the gnomonic-projection’s tangential coordinates with their zeropoint at  $RA = 84.51667$  and  $Dec = -69.14361$ , both in decimal degrees. To emulate a WFC3/UVIS frame, we applied the absolute scale for the F775W filter from Bellini et al. (2011). Small offsets and the global rotation of these transformed *Gaia* coordinates with respect to our astrometric reference catalog were eliminated by a local linear least-squares adjustment to each DR1 star using the nearest 10 common stars. This resulted in a total of 218 *Gaia* positions, ready to be added to the pool of WFC3/UVIS positions. A linear unweighted least-squares fit to the available sets of  $X$  and  $Y$  pixel positions as a function of time (and containing one *Gaia* position) provides some insights on mixing *HST* and *Gaia* positional data. First, there is a handful of outliers up to  $\sim 15$  mas possibly indicating some structure/multiplicity in the star’s image. Second, the

dispersion of *Gaia* positions in Declination at  $\sim 1.6$  mas is twice as large as that in Right Ascension, just reflecting the range of listed *Gaia* errors for these stars. Third, the *HST* WFC3/UVIS positional uncertainty for optimally exposed stars is nearing  $\sim 0.5$  mas, while the corresponding positions from DR 1 may have up to four times worse positional accuracy. Given the large disparity of positional errors in the DR 1 along each of the axes, there was little to gain from incorporating them in our dataset.

### 3. DISCUSSION AND APPLICATIONS

The primary objective of this project is to provide proper motions and the related tangential velocities for a large sample of OB stars with measured multi-epoch LOS velocities in the framework of the VFTS survey. We note that, at the distance of the LMC, a proper motion of  $0.1 \text{ mas yr}^{-1}$  is equivalent to  $25 \text{ km s}^{-1}$ . The existing measurements indicate the excess LOS velocities from VFTS data are in the range of 30 to  $\sim 100 \text{ km s}^{-1}$  (Evans et al. 2015a,b; Vink et al. 2017), or  $\sim 0.1$  to  $0.4 \text{ mas yr}^{-1}$  in the tangential plane.

Currently, this range appears to be well-established by the existing LOS velocity measurements. Now we are in the position to test them with proper motions. First, we checked for proper motions exceeding  $\sim 0.4 \text{ mas yr}^{-1}$  among all potential OB stars with emphasis on the VFTS sample. The same exercise was done for the brighter RGB stars with  $V-I > 0.9$  in order to find relatively fast moving Milky Way stars. Second, we similarly parsed the  $\sim 0.1$  to  $0.4 \text{ mas yr}^{-1}$  range but now employing the calculated and the estimated mean errors. There is a distinction between these two types of error estimates because a small number of datapoints ( $n \leq 4$ ) in the least-squares adjustment favors underestimated formal proper-motion errors. Unfortunately, many VFTS stars have this issue for our new proper motions. We note that a fit of only three datapoints was retained for stars with  $m_{F775W} < 20.0$  in order to have a proper motion estimate near the perimeter of the 30 Dor

field.

Given the fact that the accuracy of our proper motions depends on the *HST* imaging instrument, we decided to divide all 481 measured VFTS stars in three groups: proper motions from ACS/WFC (152 stars), proper motions from WFC3/UVIS observations (183 stars), and those from Paper I which do not have counterparts in our new proper motion catalog (146 stars)

### 3.1. VFTS stars and Paper I

In Paper I (Table 3) we made the first attempt to identify candidate OB runaway stars. This effort resulted in 6 such stars. Among these stars, the largest motion along either axis is  $0.40 \text{ mas yr}^{-1}$ . We note that all of them but ID 6 have their second epochs based on ACS/WFC observations. Only two OB runaway candidates (ID 1 and ID 6 = VFTS 285) have new proper motions. Star 1 (#264049) has its new proper motion incompatible with that from Paper I. We conclude that it is probably not an OB runaway. Star VFTS 285 has a consistent proper motion from both sources, albeit it appears to have a smaller newly-measured motion (see Table 1). Therefore, it remains a good candidate OB runaway. The four remaining stars are too bright to derive credible new proper motions. However, two of them (ID 3 and 4) have only one reliable position at each epoch which allows us to estimate the upper limits of proper motion. Star 3 (#278880) has inconsistent positional data and in addition has a slightly asymmetric image indicating a likely visual binary. Given the stated issues with our ACS/WFC data (Sect. 2.2), it is safer to downgrade our initial OB runaway candidates IDs 1-5 to the normal background young and massive stars.

Among the VFTS stars presented in Paper I, there are a dozen of seemingly fast moving stars outside the  $\pm 0.4 \text{ mas yr}^{-1}$  box centered on zero proper motion. An

examination of individual fits for the proper motion indicates that all but one are likely spurious. Star VFTS 712, spectral type B1 V (Evans et al. 2015a; Dunstall et al. 2015) is a nearly-equal-brightness visual binary (#290441 and #290538) separated by 228 mas, and oriented almost exactly along Declination. For both components, the proper motion in Declination appears to be fairly large but that is not confirmed by additional checks. Instructive is the case of VFTS 167, which appears to have at least a  $5\sigma$  proper motion and formally would qualify for a genuine OB runaway. However, VFTS 167 has only two good-quality datapoints at recent 2011-2014 epochs which is not sufficient to obtain any error estimates. Just a direct difference of available epoch coordinates indicates a small proper motion at  $\sim 0.2 \text{ mas yr}^{-1}$  in both axes, although with opposite sign in the RA direction to the listed one in Paper I. Clearly, its proper motion in Paper I is not reliable. Such cases are present in Paper I for two reasons: 1) the earlier-adopted cutoff magnitude included some slightly overexposed stellar images, and 2) archival *HST* frames are placed randomly in the field of 30 Dor as opposed to our design intended to optimize the astrometric output.

### 3.2. VFTS stars and ACS/WFC measurements

The vector-point diagram of ACS/WFC proper motions of 152 VFTS stars (Fig. 6) shows a fairly large scatter and a visibly non-Gaussian distribution of the smaller motions. As stated in Sect. 2.2, for brighter stars, new proper motions from ACS/WFC measurements are by a factor  $\sim 1.5$  less precise than those obtained from the WFC3/UVIS observations. We suspect that some lingering systematics in the pixel positions after correcting them for geometric distortion might be responsible for this unusual feature. Consequently, the distribution of proper motions within  $0.4 \text{ mas yr}^{-1}$  around zero is too broad to allow a meaningful identification of potential relatively-slow OB runaways. At higher proper

motions, a total of five numbered stars survive a limited scrutiny. Among them, only VFTS 838 could be a potential OB runaway (see Table 1). The remaining four stars are of late spectral type (G0-K7) and marginally consistent with the LMC membership from measured LOS velocities.

### 3.3. VFTS stars and WFC3/UVIS measurements

The sample of proper motions based upon WFC3/UVIS observations is the most accurate and reliable source of tangential velocities available from this project. As such, this sample is a cornerstone in our discussion of OB runaways and other fast moving stars. There are 183 VFTS stars in this sample. First, we exclude VFTS 680, which is apparently a G-type Milky Way star with large proper motion:  $\mu_X = +11.15 \pm 0.22$   $\mu_Y = -1.17 \pm 0.04$  mas yr<sup>-1</sup>. There is no overlap with proper motions from ACS/WFC observations, however, there are 104 proper motion measurements common with Paper I. In the majority of cases, the formal proper-motion errors are similar between Paper I and the WFC/UVIS sample of VFTS stars. Therefore, we can choose the smallest proper motion as a lower limit of the expected tangential motion, if there is a significant variation between these two sources. Normally, the preference is given to the WFC/UVIS sample because it was constructed to minimize systematic errors, which might be present in the proper motions of Paper I.

The vector-point diagram of 110 well-measured proper motions with errors  $\sigma_\mu \leq 0.13$  mas yr<sup>-1</sup> is shown in Fig. 8. There are two labeled VFTS stars standing apart from the general distribution of relative proper motions around the zero motion. Star VFTS 8 of spectral type B0.5:V(n) (Evans et al. 2015a) appears to be a candidate runaway. VFTS 245 is a K spectral type star (Evans et al. 2011) and therefore is not considered. The sum of unity Gaussians is representing the empirical 1-D proper-motion distributions in each axis and a Gaussian fit to these distributions is provided in Fig. 8 (compare that to Fig. 15,

Paper I). There are small offsets,  $\Delta\mu_X = -0.035$  and  $\Delta\mu_Y = +0.012$  mas yr<sup>-1</sup>, which along with the distribution’s Gaussian width of 0.12 mas yr<sup>-1</sup> for each axis indicate that our estimates of proper-motion errors are robust.

In order to isolate potential OB runaways, an obvious choice seems to be comparing each measured proper motion with its error and then selecting  $3\sigma$  and higher significance cases. Unfortunately, the majority of least-squares proper motion fits has a very small number of positional datapoints (Fig. 7), which brings on underestimated proper-motion errors. To mitigate this deficiency, we extracted the median error from each of the three catalogs as a function of magnitude, in four intervals of available datapoints:  $3 \leq n \leq 5$ ,  $6 \leq n \leq 7$ ,  $8 \leq n \leq 12$ , and  $n > 12$ . For example, the average median error for the VFTS stars considered here is 0.07 mas yr<sup>-1</sup>. We designed a sequence of criteria and checks that were used to identify candidate runaway stars. It is safe to reject the cases where the actual error of proper motion is more than 3 times larger than its estimated median error and use the latter as a benchmark to select potential runaway stars. In addition, we rejected the cases when the calculated proper motion errors in each axis differ by more than a factor of 3 and the number of available datapoints is only 3 or 4. This eliminates the majority of unstable solutions for proper motion. The next step is to check the consistency of proper motion between our catalog in Paper I and that from WFC3/UVIS measurements. The smallest total proper motion is thought to be more likely. An additional criterion of reliability is the sign of the proper motion, which should be the same in both catalogs. The last step is a visual inspection of the actual least-squares fit and its residuals. Finally, a runaway candidate is visually inspected on a combined image (see Sect. 4.2 in Paper I). We examined all VFTS stars which have measured proper motion in either axis exceeding 0.17 mas yr<sup>-1</sup> (equivalent to 40 km s<sup>-1</sup> at the distance of LMC). The new candidate OB runaway stars matching all our criteria, when available, are given in Table 1. This table lists VFTS number (Evans et al. 2011), identifier from our electronic table, *VI* photometry

from Cignoni et al. (2015), spectral type,  $v_{\text{LOS}}$  in  $\text{km s}^{-1}$ ,  $v \sin i$  and its error in  $\text{km s}^{-1}$ . Additional entries in Table 1 are the same as in Table 3 of Paper I. Of these six candidate OB runaways we note that only one star, VFTS 406, was flagged previously as a runaway from its LOS velocity ( $304 \text{ km s}^{-1}$ ) and high projected rotational velocity (Walborn et al. 2014), all other candidates having LOS velocities close to that of the mean of all OB stars in the region ( $\sim 270 \text{ km s}^{-1}$ ). VFTS 406 is also noteworthy due to its high rotational velocity, which would be consistent with the potential origin in the binary SN scenario for runaways; that is when one component of a binary explodes as a core-collapse supernova and the other component attains a large kick velocity. Furthermore, as we discuss in the next Sect. 3.4, this star’s direction of motion is inconsistent with an R 136 origin. In fact, only 4 stars in Table 1 have directions of motion consistent with an R 136 origin: VFTS 65, VFTS 219, VFTS 285 and VFTS 290, which are discussed further below along with the non-VFTS candidate runaways from R 136. The remaining two runaways in this sample with directions of motion inconsistent with an R 136 origin, early B-type stars VFTS 8 and VFTS 838, also have high rotational velocities that might indicate a SN ejection scenario. Another feature common to all stars listed in Table 1 is the lack of significant variations in the measured multi-epoch LOS velocities (Evans et al. 2015a; Sana et al. 2013). All of them are classed as single stars.

### 3.3.1. Candidate non-VFTS young runaways from WFC3/UVIS measurements

The VFTS survey (Evans et al. 2011) contains a total of 917 stars down to  $V = 17$ . The completeness of OB stars over the surveyed area is not well-established, especially around the location of R 136. Therefore, first we used  $VI$  photometry (Cignoni et al. 2015) and the location of the upper main-sequence in the CMD down to  $\sim 5M_{\odot}$ , equivalent to  $V \sim 19$ , and later extended that limit to  $V \sim 22$  mag. The color cut was initially

adopted at  $V - I < +0.75$  mag. This selection of targets covers the majority of young O-B-A-F spectral type main-sequence stars. Among the likely non-VFTS OB stars, only a couple of potential runaways can be tagged but none of them convincingly. At fainter magnitudes,  $18.0 < V < 22.0$ , there are a few dozen of somewhat redder stars with kinematics incompatible with LMC membership. To enhance the chances of finding *young* main-sequence stars in the area of 30 Dor, we adopted a tighter limit on the color cut at  $V - I < +0.43$ . A list of 11 potential young lower-mass runaway stars is given in Table 2. This is the first-ever such a list in a galaxy other than the Milky Way. However, membership of these stars to LMC should be confirmed by other means such as spectroscopy.

### 3.4. Candidate runaway stars and the star cluster R 136

A principal advantage of knowing proper motions of potential runaway stars is the ability to trace them backward to their place of origin, if we assume that massive star clusters are the likely nurseries of such stars. In our case, such a place is the young and massive star cluster R 136 which is located at the edge of the field covered by our WFC3/UVIS observations. We explored how the direction of proper motion vectors is oriented outwards from R 136. This can be characterized by the proper motion positional angle, measured relative to the direction from R 136. If this angle is close to zero, then there is a high probability that a star has originated from this cluster. Figure 9 show all stars from Tables 1,2. There is a distinct concentration of proper-motion positional angles around zero. We used this to identify 10 plausible escapees from R 136 (Table 3). These stars have their total proper motion in the range from 0.20 to 0.54 mas yr<sup>-1</sup> equivalent to 50 to 130 km s<sup>-1</sup>. A caveat with an actual escape velocity is that our proper motions are relative. Due to the applied chain of transformations leading to proper motions of stars in R 136 and its off-the-center position in the FOV of WFC3/UVIS, the mean proper motion of R 136

is biased towards zero. The formal proper motion of R 136 is  $\mu_X = -0.011$ ,  $\mu_Y = +0.003$  mas yr<sup>-1</sup> as calculated using the brighter and bluer stars ( $V < 22$ ,  $V - I < 0.5$ ) within one arc-minute around the center of R 136. Inspecting the rms distribution of specific WFC3/UVIS frame transformations containing the cluster (see Fig. 4), the estimated uncertainty in the proper motion of R 136 appears to be less than  $\sim 0.05$  mas yr<sup>-1</sup>.

The angular distance of an escapee and its proper motion provide the time when the star left R 136. Thus, the slowest escapees – VFTS 285 and VFTS 290 – have moved to the current position in 0.67 Myr. Star VFTS 65 has traveled 1.37 Myr and has covered 92 pc away from R 136. If the isochrone age of R 136 age is considered (3 Myr, Cignoni et al. 2015), then a potential early escapee with a mass of  $\sim 20M_\odot$  or higher may have traveled as far as  $\sim 200$  pc away from R 136, equivalent to the length of  $\sim 14'$  in the tangential plane. We note that the LOS velocities of VFTS stars imply the runaway upper limit at  $\sim 100$  km s<sup>-1</sup> (Vink et al. 2017). That would result in a distance of  $\sim 300$  pc ( $\sim 20'$ ) over 3 Myr. *Gaia* proper motions will enable searches for ejected runaways from R 136 at these greater distances from the cluster.

For those stars with position angles consistent with ejection from R 136 that are also in the VFTS sample (stars VFTS 65, 219, 285 and 290), we can compare their evolutionary ages (Schneider et al. 2018) with the age of the central cluster, estimated to be 1.5 Myr (Crowther et al. 2016). The O-type stars VFTS 65 and 285 have ages estimated at 2.4 and 1.9 Myr, respectively with uncertainties of approximately 1 and 2 Myr, hence they have ages consistent with that of R 136. The remaining confirmed O-type star, VFTS 290, has an age of 4.7 Myr with an uncertainty of approximately 0.5 Myr. Furthermore, from the analysis of Sabín-Sanjulián et al. (2017) it appears that to match the age R 136 this object would have to be a  $\sim 3\sigma$  outlier. Since this star has an age that is more consistent with the surrounding NGC 2070 cluster it may well be that this runaway is the product of the binary

supernova mechanism (Blaauw 1961) and originated in that region. The case of VFTS 219 is even more problematic as this mid-B star has an estimated age of 77 Myr and, while the uncertainty is  $\sim 10$  Myr, this star is inconsistent with previous membership of R 136. We suggest that VFTS 219 (and potentially even VFTS 290) might be an interloper in the sense that it is a field runaway star that by chance has a position angle consistent with ejection from R 136. Indeed, referring to the histogram in Fig. 9 one can see that we expect approximately one star per 33 degree bin of position angle, irrespective of the bin’s orientation with respect to R 136. In the central 3 bins we therefore expect about 3 stars that might be interlopers in our sample.

Among the more massive escapees, we note a pair of main sequence O-stars (VFTS 285 & VFTS 290) which are separated only by  $4''.27$ . Their total proper motion is identical but not the LOS velocities and projected rotation velocities: 228 and 269 km s $^{-1}$  (Sana et al. 2013);  $v \sin i$ : 600 and 40 km s $^{-1}$  (Sabín-Sanjulián et al. 2017). According to Evans et al. (2015a), the mean LOS velocity of NGC 2070, which also contains R 136, is 271 km s $^{-1}$ . From the perspective of LOS velocities, only VFTS 285 appears to be a runaway star, albeit of a slow variety. However, our proper motion measurement of these stars appears to be fairly robust, hence confirming their runaway status. It is unlikely that this pair is a wide physical binary due to the very large current projected separation in the tangential plane at  $\sim 213,000$  AU.

Another potential runaway pair, #371614 and VFTS 662, is even less understood. In Table 2, star #371614 is listed as a candidate runaway. Its orientation angle with respect to R 136 is  $-144$  deg. Formally, that large angle rules out any connection to this star cluster. However, the derived proper motion appears to be biased by the nearby and more luminous VFTS 662 (separated by  $\sim 0''.3$ ), which is missing in our catalogs. According to Evans et al. (2015a), VFTS 662 has its LOS velocity at 251 km s $^{-1}$ . It is expected that *Gaia* DR 2 will

help to clarify the status of this pair.

An additional argument that our candidate escapees from R 136 are real comes from the distribution of redder main-sequence ( $0.43 < V - I < 0.75$ ) runaway stars down to  $V = 22$  mag. There are 34 such stars shown in Fig. 10. The histogram of positional angles implies a lack of concentration at the zero orientation angle. We note that for the faster-moving stars this concentration would be much sharper due to the greatly diminished impact of proper motion errors. In addition, the amplitude of the total proper motion in this sample is much larger – from 0.4 to more than 4 mas yr<sup>-1</sup>, indicating very different kinematics.

These two sets of kinematically-selected stars also have a very different placement on the  $V - I$  vs.  $V$  CMD (Fig. 11) where the interchangeable axes are labeled  $F555W$  vs.  $F555W-F775W$  in accordance with Cignoni et al. (2015). The 10 escapees are well-separated from fast-moving field stars. The stars likely escaped from R 136 are located along the main sequence of this young cluster down to its pre-main-sequence. As expected, the remaining 8 candidate O-B-A-F runaways not emanating from R 136 are fairly close to the location of R 136 escapees. The fast-moving field stars form a vertical sequence, similar to that toward the north Galactic pole (Reid & Majewski 1993). Apparently, these are Milky Way halo stars at various distances from the Sun. To illustrate this point, we overplotted an appropriate isochrone which fits well the most distant stars, and which are also kinematically slowest in our sample as indicated by their total proper motion. There is an ambiguity, though, to which population we should assign three isolated stars at  $V \sim 21.7$  and  $V - I \sim 0.43$ . Therefore, their status remains undefined.

There is an intriguing relationship for the likely-escaped stars from R 136 – their total proper motion (see Table 3) is correlated with the apparent  $V$ -magnitude (Fig. 12). Since these stars are located approximately at the same distance from the Sun, their apparent

magnitudes become akin to absolute magnitudes and can be used as a proxy of mass for main-sequence stars. Clearly, less massive stars are moving faster, which is contrary to what is expected in most dynamical ejection scenarios (e.g., Oh et al. 2015; Oh & Kroupa 2016) where the more massive runaways tend to have higher velocities. Perusing various simulations performed by Oh & Kroupa (2016), it appears that certain models do predict a trend of increasing velocity with decreasing mass. For example, in those scenarios that assume a random pairing of binary masses among the initial conditions that trend is further strengthened when the initial conditions assume the cluster is not mass-segregated (models MS3RP and NMS3RP of Oh & Kroupa (2016)). However, we also note that the absence of faint runaways with smaller proper motions in Fig. 12 is somewhat baffling. For stars fainter than  $V = 19$ , the detection limit in total proper motion is  $\sim 0.3 \text{ mas yr}^{-1}$ . The range 0.2-0.3  $\text{mas yr}^{-1}$  for these stars was not carefully explored owing to the large number of impostors and our inability to identify bona fide cases. Therefore, it is appropriate to assert that we did not find any faster-moving massive escapee, which could match the maximum escape velocities of less massive stars.

A potential issue with the interpretation of this correlation with the mass might be neglecting the contribution of excess LOS velocity relative to the mean motion of R 136. In fact, for three massive stars out of four, that contribution is negligible (see Table 1). For star VFTS 285, the total escape velocity would be an equivalent of  $0.27 \text{ mas yr}^{-1}$ . That alone cannot change significantly the slope shown in Fig. 12. VFTS 285 has an extremely high  $v_{\text{sin}i}$  estimate which makes the measurement of LOS velocity nontrivial. However, Sana et al. (2013) provide 7 independent and mutually consistent estimates of LOS velocities for VFTS 285.

The same trend as a function of  $V$ -magnitude can be detected among the 8 candidate young O-B-A-F runaways not related to R 136. However, with the exception of VFTS 406,

their total proper motion is significantly higher (by 0.1-0.15 mas yr<sup>-1</sup>, or 25-40 km s<sup>-1</sup>) than that shown in Fig. 12. This is puzzling considering that the proper-motion errors in both samples are similar. It is tempting to identify this sample of runaways and, as discussed above, even some stars in the R 136 runaway sample as the products of the binary supernova ejection (BSE) scenario. These would be relatively fast runaways, with tangential speeds in the range 50-100 km s<sup>-1</sup>. It is not straightforward to estimate the fraction of OB stars that are BSE runaways given the incompleteness of detections in the ACS/WFC data, the bright magnitude limit that excludes many O-stars, and the unknown incompleteness of the astrometric catalog. However 4 of our 8 BSE candidates are OB-type stars, and we detected 481 known OB stars in our catalog. This implies an upper limit of around 1% as the fraction of fast OB runaways. Given the various caveats referred to above this is not inconsistent with model predictions of runaway fractions of at most a few percent (Eldridge et al. 2011; Renzo et al. 2018) although their definition of a runaway adopts a peculiar velocity of greater than 30 km s<sup>-1</sup>.

However we refrain here from deeper analysis and interpretation for two reasons: 1) our best proper motions cover a limited  $\sim 15' \times 7'$  area only partially overlapping with R 136; and 2) our observations cannot provide reliable proper motions for stars brighter than  $V \sim 15$ , while luminous O-type supergiants in the 30 Dor area can be as bright as magnitude  $V \sim 11$  (Selman et al. 1999). A full analysis and interpretation is planned once the sample can be augmented by new *Gaia* DR2 proper motion measurements.

#### 4. CONCLUSIONS

We derived a new proper motion catalog based on dedicated WFC3/UVIS and parallel ACS/WFC observations. Combined with the data from our pilot archival study, we provide proper motions for 368,787 stars in the region of 30 Dor. Among the stars brighter than

$V \sim 22$  mag, a number of fast moving stars are identified. A total of 10 runaway stars have proper motion directions consistent with an origin in the young and massive star cluster R 136, albeit roughly one third of these may be chance alignments. Our WFC3/UVIS observations provide the necessary accuracy to detect reliable proper motions in the range of  $\sim 0.15$  to  $0.5 \text{ mas yr}^{-1}$  where the O-B-A-F runaways were identified. This is a unique sample of runaway stars allowing us to better understand the process of dynamical ejection of stars in very young clusters, and to put realistic limits on the rate of such ejections.

In summary, the main achievements of this study are:

1. We detail an empirical approach to account for differential Charge-Transfer Inefficiency, which is similar for both *HST* imaging instruments – ACS/WFC and WFC3/UVIS.
2. We calculated relative proper motions for a total of 368,787 stars down to  $V \sim 25$ . This second high-accuracy proper motion catalog in the region of 30 Dor is instrumental to explore young fast-moving stars.
3. We did not find any fast moving OB star (with total proper motion  $\mu > 0.4 \text{ mas yr}^{-1}$ , equivalent to  $\sim 100 \text{ km s}^{-1}$ ) among a total of 481 measured VFTS stars. That may rule out some suggested pathway(s) for creating runaway stars in clusters. We predict that all the more massive runaways (mass higher than  $\sim 20M_{\odot}$ ), originating from the young and massive star cluster R 136, will be found within 200-300 pc from R 136.
4. All candidate OB proper-motion runaway stars are single and most of them have high projected rotation velocities, including a record-high VFTS 285 at  $v \sin i = 600 \text{ km s}^{-1}$ .
5. There is convincing evidence that a number of O spectral-type down to F-stars have escaped from R 136. It appears that these escapees have tangential velocities

correlated with apparent magnitude, which points to the stellar mass as a driver for the escape velocity distribution.

The authors gratefully acknowledge grant support for programs GO-12499, GO-12915, and GO-13359, provided by NASA through grants from the Space Telescope Science Institute, which is operated by the Association of Universities for Research in Astronomy, Inc., under NASA contract NAS 5-26555. We thank co-investigators Nate Bastian and Eli Bressert for their support in the construction of this proposal. IP thanks Jay Anderson, Terrence Girard, and Rosemary Wyse for insights on astrometry from saturated images, discussions on error propagation issues, and for clarification on the properties of various stellar populations. DJL would like to acknowledge the critical and enthusiastic contribution made by our departed and greatly missed colleague, Nolan Walborn.

*Facilities:* Hubble Space Telescope

## REFERENCES

- Anderson, J., & King, I. R. 2000, *PASP*, 112, 1360
- Anderson, J., & King, I. R. 2003, *PASP*, 115, 113
- Anderson, J., & Bedin, L. R. 2010, *PASP*, 122, 1035
- Bellini, A., Anderson, J., Bedin, L. R. 2011, *PASP*, 123, 622
- Blaauw, A. 1961, *BAN*, 15, 265
- Cignoni, M., Sabbi, E., van der Marel, R. P., et al. 2015, *ApJ*, 811:76
- Crowther, P. A., Caballero-Nieves, S. M., Bostroem, K. A., et al. 2016, *MNRAS*, 458, 624
- Dunstall, P. R., Dufton, P. L., Sana, H., et al. 2015, *A&A*, 580, A93
- Eldridge, J. J., Langer, N., Tout, C. A. 2011, *MNRAS*, 414, 3501
- Evans, C. J., Taylor, W. D., Hénault-Brunet, V., et al. 2011, *A&A*, 530, A108
- Evans, C. J., Kennedy, M. B., Dufton, P. L., et al. 2015, *A&A*, 574, A13
- Evans, C. J., van Loon, J. Th., Hainich, R., & Bailey, M. 2015, *A&A*, 584, A5
- Gaia Collaboration, Brown, A. G. A., Vallenari, A., et al. 2016, *A&A*, 595, A2
- Lennon, D. J., van der Marel, R. P., Ramos Lerate, M., O’Mullane, W., Sahlmann, J. 2017, *A&A*, 603, A75
- Kozhurina-Platais, V., Borncamp, Anderson, J. 2015, Instrument Science Report ACS 2015-06, (Baltimore: STScI)
- Oh, S., Kroupa, P., & Pflamm-Altenburg, J. 2015, *ApJ*, 805, 92

- Oh, S., & Kroupa, P. 2016, *A&A*, 590, A107
- Platais, I., van der Marel, R. P., et al. 2015, *AJ*, 150:89
- Ramírez-Agudelo, O. H., Sana, H., de Koter, A., et al. 2017, *A&A*, 600, A81
- Reid, N., & Majewski, S. R. 1993, *ApJ*, 409, 635
- Renzo, M., de Mink, S. E., Zapartas, E., et al. 2018, *å*, to be submitted
- Sabbi, E., Lennon, D. J., Anderson, J., et al. 2016, *ApJS*, 222:11
- Sana, H., de Koter, A., de Mink, S. E., et al. 2013, *A&A*, 550, A107
- Sabín-Sanjulián, C., Simón-Díaz, S., Herrero, A., et al. 2017, *A&A*, A79
- Selman, F., Melnick, J., Bosch, G., & Terlevich, R. 1999, *A&A*, 341, 98
- Schneider, F. R. N., Sana, H., Evans, C. J., et al. 2018, *Science*, 359, 69
- Vink, J. S., Evans, C. J., Bestenlehner, J., McEvoy, C., et al. 2017, in *Proceedings of the IAU Symposium 329: The Lives and Death-Throes of Massive Stars*, ed. J. J. Eldridge, J. C. Bray, L. A. S. McClelland, & Lin Xiao, 279
- Walborn, N. R., Sana, H., Simón-Díaz, S. et al. 2014, *A&A*, 564, A40

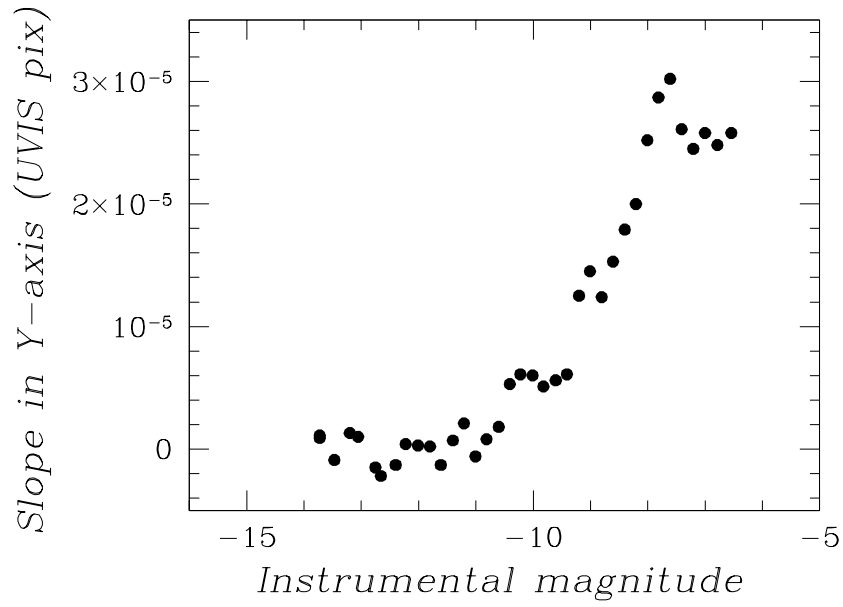


Fig. 1.— Example of differential-CTE slope distribution as a function of instrumental magnitude. It is for WFC3/UVIS Chip 1 and short exposures only, which produced a total of nearly 20K residuals.

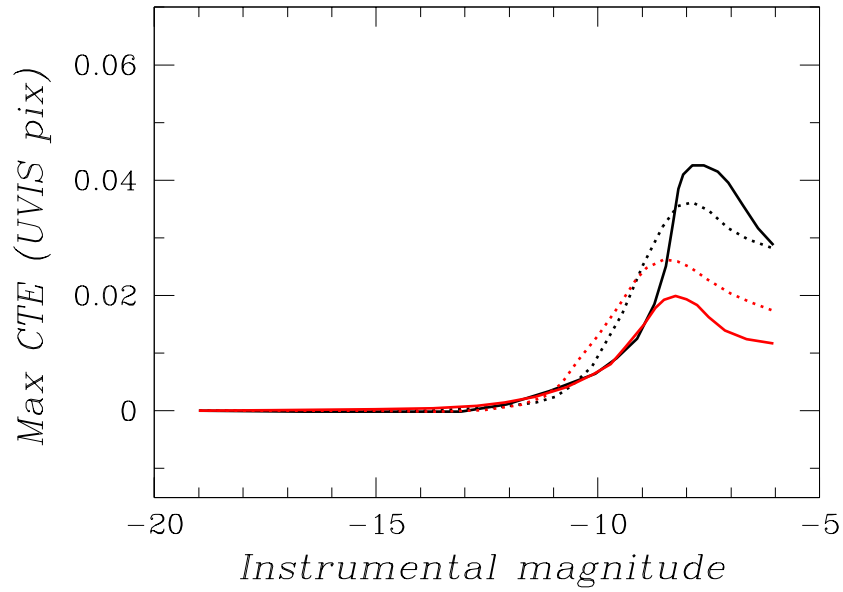


Fig. 2.— Maximum effect of differential CTE for ACS/WFC as a function of magnitude, chip selection, and exposure length. Solid lines represent WFC1; dotted lines – WFC2. Black lines shows the effect for short 32 s exposures; red lines – for long 640 s exposures.

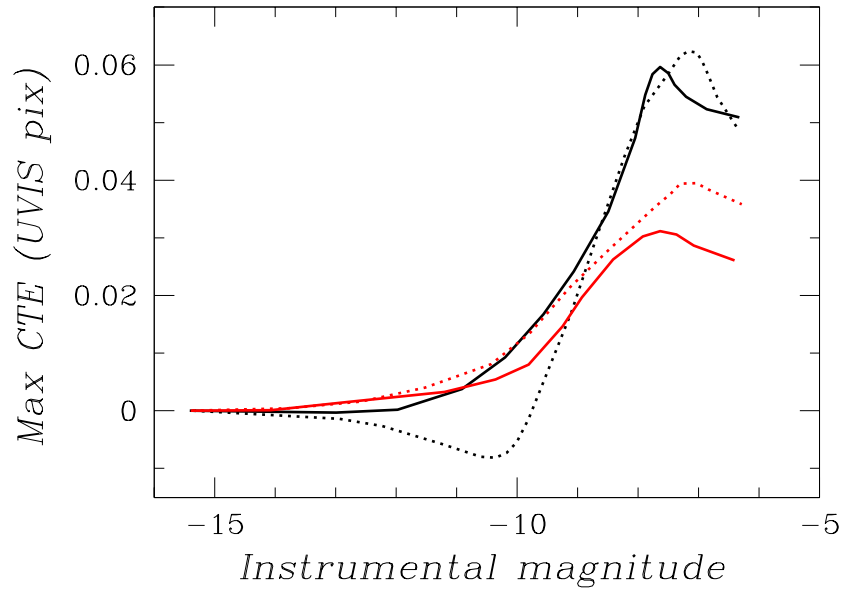


Fig. 3.— Maximum effect of differential CTE for WFC3/UVIS as a function of magnitude, chip selection, and exposure length. Solid lines represent Chip 1; dotted lines – Chip 2. Black lines shows the effect for short 35 s exposures; red lines – for long 699 s exposures.

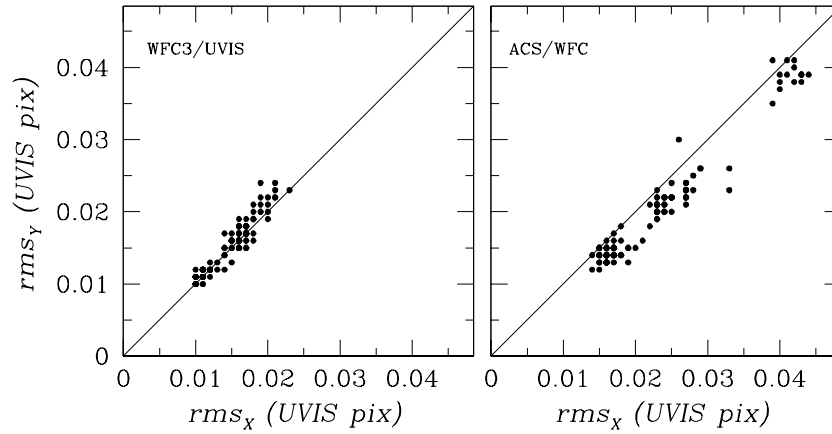


Fig. 4.— Distribution of rms from the least-squares linear transformation of individual frames into the astrometric reference catalog. The reason of the worse rms for ACS/WFC frames is discussed in Sect. 2.2. There is a total of 149 rms estimates for each of the *HST* imaging instruments.

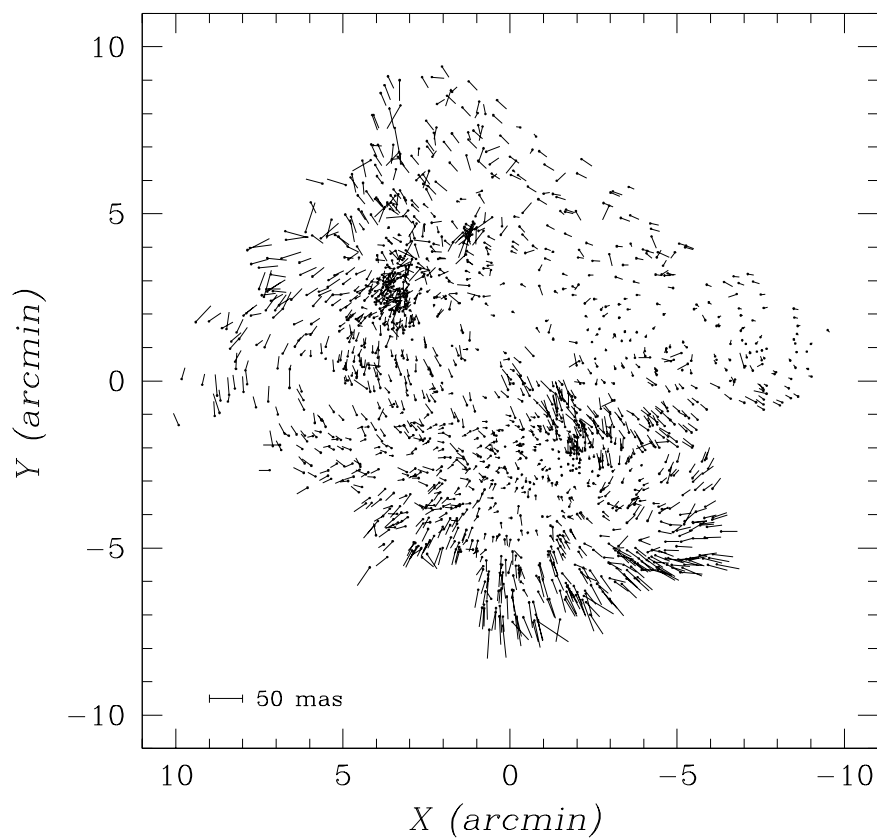


Fig. 5.— Positional residuals of 1738 stars common between the *Gaia* DR 1 and our astrometric reference catalog. These residuals were obtained using a linear least-squares adjustment. The part of the sky covered by ACS/WFC observations is most affected by systematic errors. These absolute residuals do not affect our proper motion measurements, which are based on relative local comparisons between observing epochs.

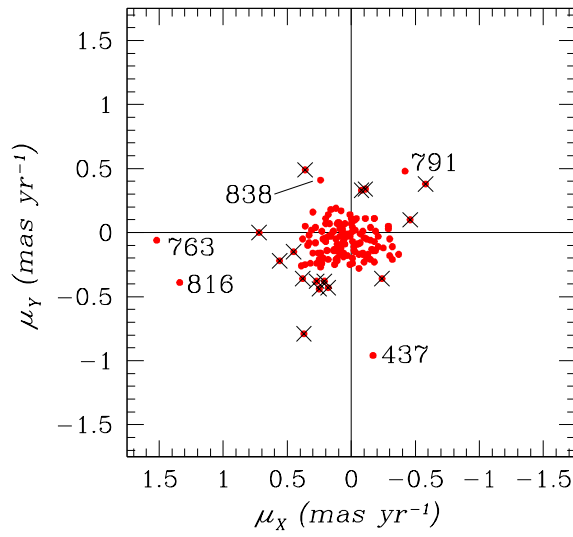


Fig. 6.— Vector-point diagram of ACS/WFC-based proper motions for VFTS stars. The status of labeled stars is discussed in Sect. 3.2. Inconsistent or apparently flawed proper motions are crossed out. This diagram yields only a single candidate OB runaway (VFTS 838).

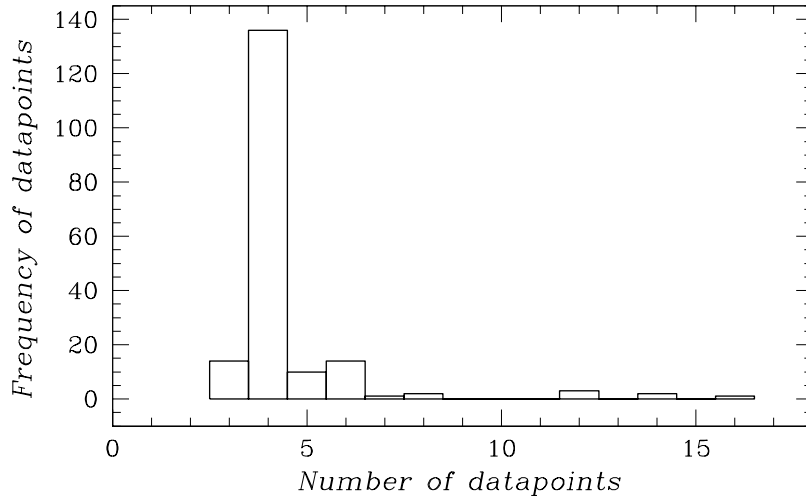


Fig. 7.— Histogram of the number of positional datapoints for VFTS stars used in the WFC3/UVIS proper motion measurements.

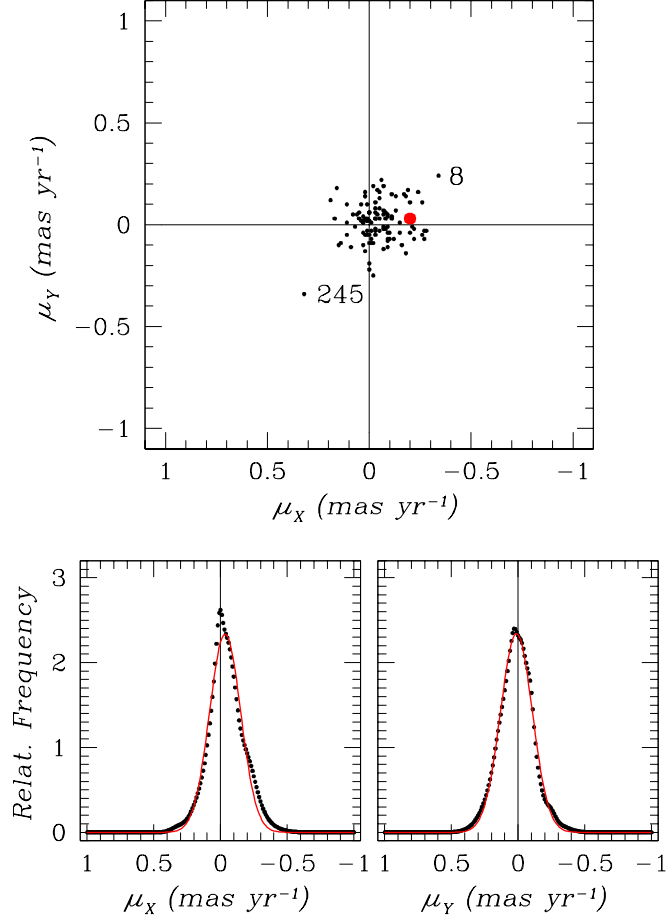


Fig. 8.— Proper motions of 110 VFTS stars from the WFC3/UVIS measurements. Only proper motions with errors  $\sigma_\mu \leq 0.13$  mas yr $^{-1}$  are selected. Upper panel: a vector-point diagram. The status of two labeled stars is discussed in Sect. 3.3. The likely OB runaway star VFTS 285 is marked in red. Bottom panels: black points represent empirical 1-D distributions of proper motions; red points show a Gaussian fit to these distributions yielding a width of 0.12 mas yr $^{-1}$  and indicating small offsets.

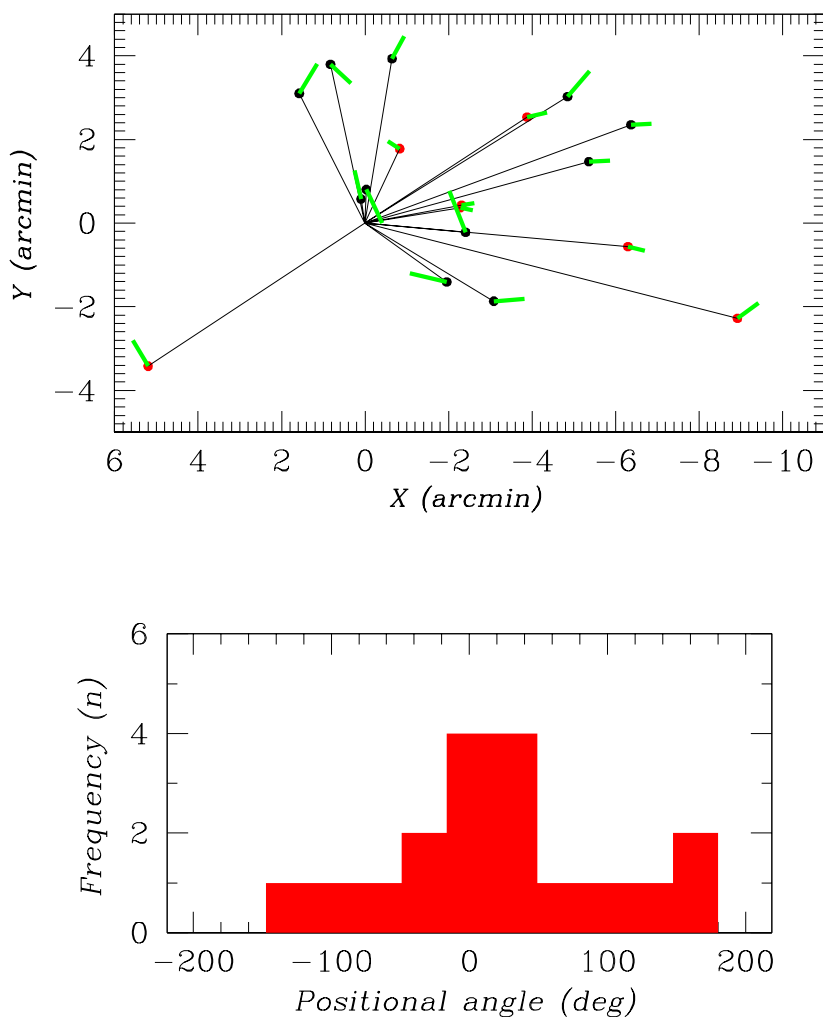


Fig. 9.— Distribution of 18 candidate runaway stars. Upper panel: location of stars on the sky. Red dots indicate OB stars while black points show the likely young A-F spectral type stars. The zeropoint of gnomonic projection is at the center of the rich and young star cluster R 136. Green line-segments indicate the direction and amount of a star’s proper motion ( $1.5 \text{ mas yr}^{-1}$  corresponds to  $1'$ ). Bottom panel: histogram of proper-motion positional angle with respect to the direction outwards from R 136 (thin black lines). The size of a bin is  $33 \text{ deg}$ . There is a distinct concentration around zero angle, which is a hallmark of genuine runaway stars.

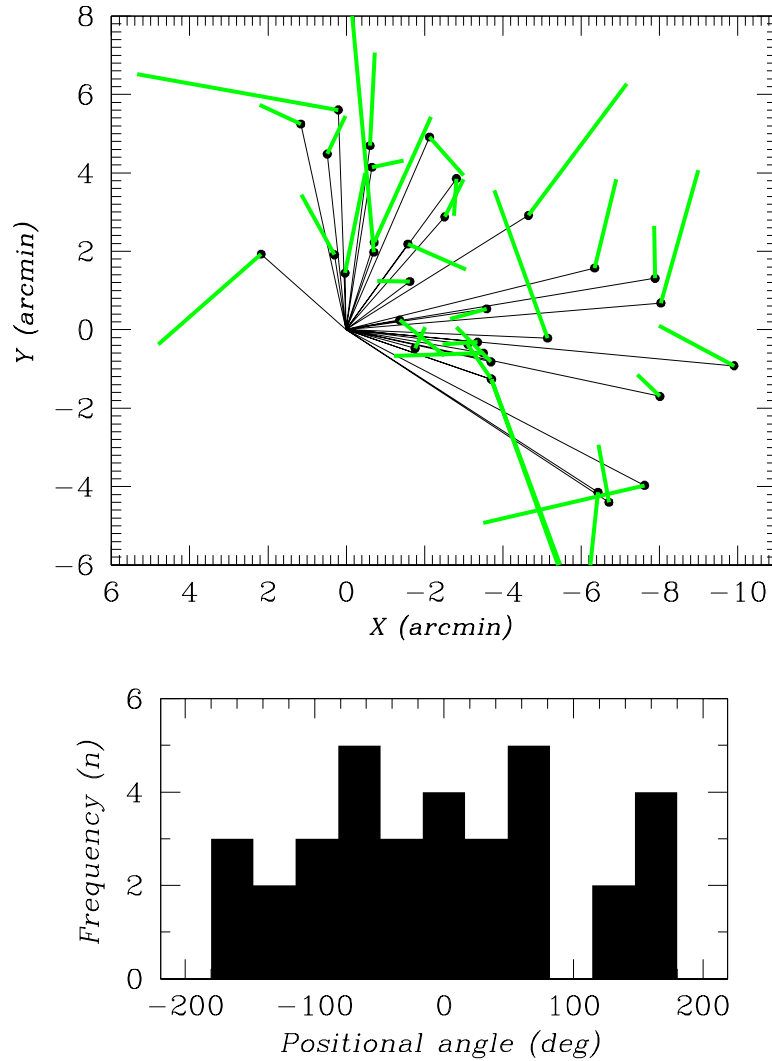


Fig. 10.— Distribution of fast-moving field stars. This plot is identical to Fig. 9 but addresses the redder main-sequence stars which on average have much higher proper motions and a random distribution of positional angles. The proper-motion amplification factor used for visualization is identical to that used in Fig. 9.

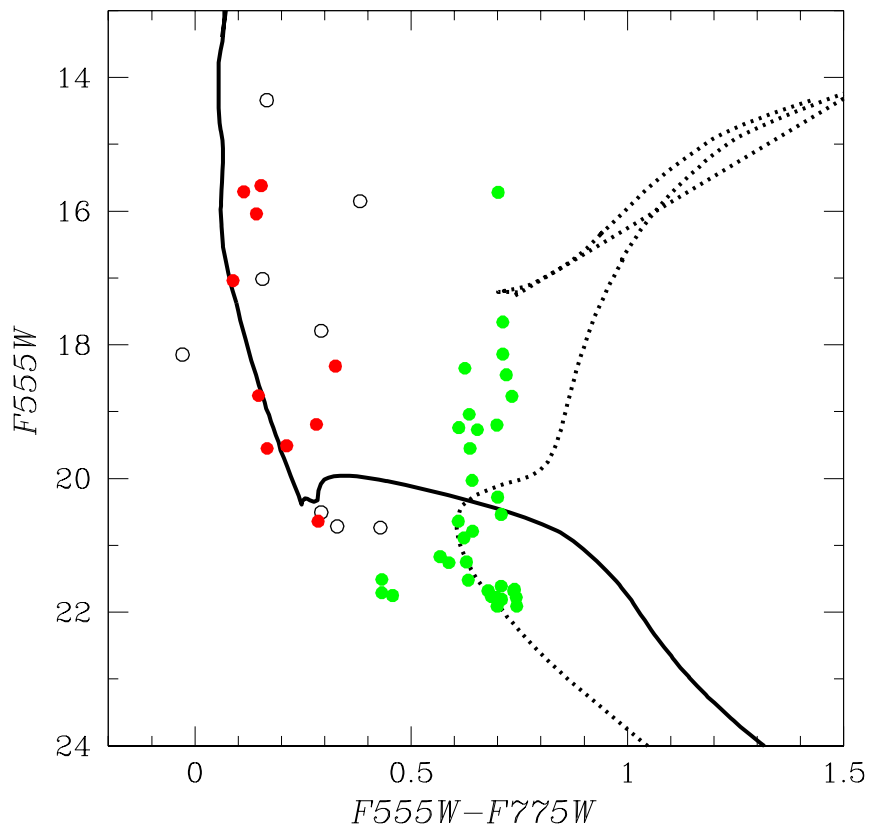


Fig. 11.— Color-magnitude diagram of the stars plotted in Figs. 9,10. Red points – all stars from Table 3; open circles – candidate O-B-A-F runaways not kinematically-associated with R 136; green points - fast moving field stars. Solid curved line is the 3 Myr isochrone for the cluster R 136, adopting  $E(B - V) = 0.3$ . The dotted line shows an isochrone with the following parameters: 12 Gyr old, metal-poor  $[Fe/H] = -1.5$  dex,  $E(B - V) = 0.05$ , and placed at 20 kpc from the Sun.

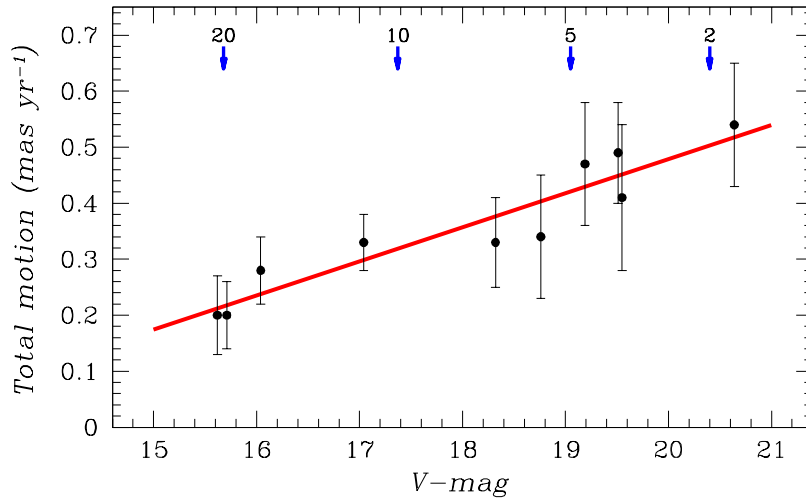


Fig. 12.— Total motion of runaway stars consistent with escaping from R 136. There is a correlation of total motion with the stellar magnitude which acts as a proxy of stellar mass. The latter in solar units is indicated by a down-pointed arrow at four locations of the magnitude axis. The slope of this distribution is  $0.061 \pm 0.008$  mas yr<sup>-1</sup> per unit magnitude.

**Table 1.** Candidate OB proper-motion runaway stars

VFTS	Ident	$V$	$V - I$	Sp. Type	$v_{\text{LOS}}$	$vsini$	$\mu_X$	$\mu_Y$	$\sigma_{\mu_X}$	$\sigma_{\mu_Y}$	$\chi_X^2$	$\chi_Y^2$	$Q_X$	$Q_Y$	$N_{\text{frame}}$
8	188822	17.014	0.156	B0.5 V(n)	271	241±15	-0.34	0.24	0.10	0.10	0.27	0.28	0.899	0.899	6
65	259107	16.036	0.142	O8 V(n)	268	162±20	-0.27	-0.07	0.06	0.09	0.06	0.14	0.814	0.706	3
219	349614	17.043	0.088	B3-5 III-V	282	220±19	-0.32	0.07	0.04	0.15	0.04	0.62	0.996	0.646	6
285	294979	15.616	0.052	O7.5 Vnnn	228	600±??	-0.20	0.03	0.07	0.12	0.13	0.37	0.877	0.687	4
290	292849	15.708	0.113	O9.5 IV	269	<40	-0.20	-0.04	0.06	0.06	0.09	0.09	0.914	0.915	4
406	332741	14.340	0.166	O6 Vnn	304	356±30	0.19	0.12	0.05	0.06	0.06	0.06	0.946	0.944	4
838	143204	15.852	0.382	B1: II(n)	263	239±23	0.24	0.41	0.20	0.11	1.03	0.29	0.355	0.750	4

TABLE 2. CANDIDATE YOUNG A-F PROPER-MOTION RUNAWAYS

Ident	$V$	$V - I$	$RA$ (deg)	$Dec$ (deg)	$\mu_X$	$\mu_Y$	$\sigma_{\mu_X}$	$\sigma_{\mu_Y}$	$\chi_X^2$	$\chi_Y^2$	$Q_X$	$Q_Y$	$N_{\text{frame}}$
204988	19.509	0.212	84.5362650	-69.1332743	-0.49	0.04	0.09	0.12	0.25	0.50	0.958	0.810	8
223800	17.790	0.292	84.5887628	-69.1256231	0.59	0.14	0.04	0.08	0.03	0.12	0.971	0.888	4
271782	20.508	0.292	84.5679256	-69.1058476	0.26	0.66	0.10	0.07	0.72	0.34	0.721	0.978	13
299597	19.188	0.281	84.6849573	-69.0926151	0.10	0.46	0.09	0.11	0.43	0.64	0.901	0.747	10
306820	20.717	0.329	84.6791949	-69.0887983	-0.26	-0.54	0.12	0.06	0.69	0.14	0.739	0.999	12
325244	18.757	0.147	84.4301820	-69.0775362	-0.34	0.02	0.11	0.06	1.22	0.41	0.248	0.978	17
346142	18.324	0.325	84.3832657	-69.0627707	-0.33	0.02	0.08	0.06	0.47	0.34	0.936	0.981	12
358858	20.637	0.285	84.4541695	-69.0516393	-0.35	0.41	0.11	0.11	0.77	0.75	0.778	0.704	14
359942	20.735	0.429	84.7538538	-69.0505241	-0.29	0.47	0.17	0.10	1.31	0.43	0.234	0.904	14
371614	18.147	-0.029	84.7191400	-69.0389415	-0.33	-0.30	0.07	0.10	0.27	0.53	0.977	0.833	10
373715	19.546	0.167	84.6501694	-69.0366983	-0.19	0.36	0.11	0.14	0.90	1.35	0.545	0.183	14

Table 3. Likely-escaped stars from R 136

Ident	X (arcmin)	Y (arcmin)	Angle (deg)	Total pm (mas yr <sup>-1</sup> )
204988	-3.0804	-1.8681	35.9	0.49
259107	-6.3002	-0.5612	-9.4	0.28
292849	-2.2820	0.3702	-20.5	0.20
294979	-2.3160	0.4293	-2.0	0.20
299597	0.0976	0.5751	2.6	0.47
325244	-5.3612	1.4689	-12.0	0.34
346142	-6.3708	2.3503	-16.8	0.33
349614	-3.8849	2.5365	-20.8	0.33
358858	-4.8530	3.0247	17.6	0.54
373715	-0.6489	3.9299	-18.4	0.41